Article

The Application of Tsallis Entropy Based Self-Adaptive Algorithm for Multi-Threshold Image Segmentation

Kailong Zhang , Mingyue He , Lijie Dong , Congjie Ou *

Posted Date: 7 August 2024

doi: 10.20944/preprints202408.0511.v1

Keywords: Tsallis Entropy; Long-range Correlations; Self-adaptive Algorithm; Multi-level Thresholding; Robustness

 doi:10.20944/preprints202408.0511.v1

Article

The Application of Tsallis Entropy Based Self-Adaptive Algorithm for Multi-Threshold Image Segmentation

Kailong Zhang, Mingyue He, Lijie Dong and Congjie Ou *

College of Information Science and Engineering, Huaqiao University, Xiamen 361021, China; 22014082032@stu.hqu.edu.cn(K.Z.);
* Correspondence: jcou@hqu.edu.cn

Abstract: Tsallis entropy has been widely used in image thresholding because of its non-extensive properties. The non-extensive parameter q contained in this entropy plays an important role in various adaptive algorithms and has been successfully applied in bi-level image thresholding. In this paper, the relationships between parameter q and pixels' long-range correlations have been further studied within multi-threshold image segmentation. It is found that the pixels' correlations are remarkable and stable for images generated by a known physical principle, such as infrared images and medical CT images. And the corresponding non-extensive parameter q can be evaluated by using self-adaptive Tsallis entropy algorithm. The results of this algorithm are compared with those of Shannon entropy algorithm and the original Tsallis entropy algorithm, in terms of quantitative image quality evaluation metrics PSNR (Peak Signal-to-Noise Ratio) and SSIM (Structural Similarity). Furthermore, we observed that for image series with the same background, the q values determined by the adaptive algorithm are consistently kept in a narrow range. Therefore, similar or identical scenes during imaging would produce similar strength of long-range correlations, which provides potential applications for unsupervised image processing.

Keywords: Tsallis entropy; long-range correlations; self-adaptive algorithm; multi-level thresholding; robustness

1. Introduction

In recent years, with the increasing of digital imaging devices, the image data grows rapidly. Therefore, image processing becomes more and more crucial in machine vision. During image processing, image segmentation is a fundamental step that divides an image into different regions by means of intensity, color, contour and so on. It has been successfully used in various fields[1–4] and the achievements are still growing. Technically, image segmentation mainly contains threshold-based segmentation, edge-based segmentation[5], clustering-based segmentation[6], and region-growing segmentation[7]. The threshold-based image segmentation becomes the most frequently used method due to its simplicity, efficiency, and stability.

In 1980, Pun[8] firstly applied information entropy to image thresholding and it has been improved by Kapur[9], who proposed Maximum Shannon Entropy Thresholding algorithm. Kapur's main idea is to treat the digital gray-level image as a matrix that contains pixels with different gray-level value. The gray-level histogram of the pixels can be considered as a kind of probability distribution. The entropy of the gray-level distribution can be maximized by a proper threshold, which is similar to maximize the contrast between object and background of the image. If two or more objects exist in the same background, resulting in a multimodal gray-level distribution, the above mentioned algorithm can be naturally extended to multi-threshold segmentation. It is worth noting that with the increasing number of thresholds, the computational complexity grows exponentially. In order to overcome this complexity and yield the optimal multi-threshold solution, swarm intelligence optimization algorithms are frequently used to solve such problems[10–15].

The concept of entropy was firstly proposed in thermo-statistical physics to deal with extensive systems[16]. Shannon entropy[17] inherits the extensivity and has been widely used in information theory. However, there are a lot of complex systems that presenting long-range interactions and the extensivities of them are broken. Extensive entropies are unsuitable to describe such systems any more.

 doi:10.20944/preprints202408.0511.v1

Tsallis indicates a generalized entropic form[18] for those systems and the abnormal behaviors of them are well fitted by the non-extensive parameter q. Over the years, Tsallis entropy has been applied not only in physics[19], but also in financial markets[20], seismology[21], bioinformatics[22], fractal networks[23], and so on. Regarding image segmentation, Tsallis entropy shows high adaptability for different types of targets recognition[24–26] since the non-extensive parameter q is related to the strength of long-range correlations among image pixels. However, to determine an appropriate value of q for a given image is still an open question in practice, since different types of images may present different patterns of correlations among pixels. Generally, the estimation of q values are performed empirically[27,28] in Tsallis entropy based image segmentation, and the relationships between q values and the pixels' correlations need to be further discussed.

In 2009, Paulo S et al.[29] proposed a method to yield the optimal q values of images by maximizing the difference between q-dependent entropy and the upper limit of the histogram entropy, which sheds light on the patterns recognition of the pixels' long-range correlations. In 2016, Abdiel et al.[30] provided another method to obtain the non-extensive q values. It is based on the concept of redundancy in information theory and the entropy maximization principle, and has been successfully applied to the bi-level image thresholding[31]. While extending the bi-level segmentation to multi-level cases, with the increasing number of objects at different gray-level, the patterns of the pixels' long-range correlation may also increase. In order to avoid the perturbations from uncertain interactions among pixels, the images generated by unified imaging process should be adopted to illustrate the relationships between q value and the long-range correlations of pixels. The rest of this paper is organized as follows. Section 2 briefly review the q-redundancy maximization method and introduce the application of it in multi-level image segmentation. In Section 3, according to the known physical principles, six image datasets are adopted for testing, and the quantitative image quality evaluation metrics such as PSNR and SSIM are introduced within multi-level image segmentation. In Section 4, the statistical results of different image datasets are illustrated so that the relationships between q-values and pixels' long-range correlations are further discussed. In Section 5, the conclusions are presented.

2. Methods for Calculating Tsallis Entropy Index q and Image Segmentation

Assuming a given image size is $M \times N$, representing the total number of pixels in it. The range of gray-level of the image is defined as $i = 0, 1, 2, ..., L-1$, where L represents the maximum gray-level of the image, such as 256. Thus, the gray-level probability distribution of the image is defined as:

$$p_i = \frac{h_i}{M \times N}, \tag{1}$$

where h_i is the number of pixels that the gray-level value is equal to i, and $p_i \geq 0, \sum_{i=0}^{L-1} p_i = 1$ hold. Obviously, $\{p_i\}$ represents the gray-level histogram distribution of the image. And Tsallis entropy is written as[18,19,24,32]:

$$S_T = \frac{1 - \sum_i p_i^q}{1 - q}, \tag{2}$$

where q is the non-extensive index.

2.1. Entropy Index q and The Long-Range Correlation

Abdiel et al. suggest that each complex system has its own entropy index, and it should not be determined arbitrary. In practice, an image can be considered as a non-extensive pixel system so that the long-range correlations among them can be quantified by q. Therefore, two fundamental concepts, redundancy and the maximum entropy principle, play important roles in evaluating the non-extensive

 doi:10.20944/preprints202408.0511.v1

parameter q. According to the non-extensive properties of Tsallis entropy, the q-redundancy of an image's histogram can be written as[30]:

$$R_T = 1 - \frac{S_T}{S_{T\max}}, \tag{3}$$

where $S_{T\max} = \frac{1-L^{1-q}}{q-1}$. It means that the entropy reaches its maximal at equiprobability case, i.e., $p_i = p_j = 1/L \ (\forall i, j)$. For a given image with known gray-level histogram, the corresponding q-redundancy can be adjusted by parameter q. On the other hand, the histogram may exhibit long-range correlations among the pixels of the image. Therefore, maximizing the q-redundancy is a hopeful way to recognize the pattern of long-range correlations and yields a suitable non-extensive parameter q, i.e.:

$$q^* = \arg\max(R_T). \tag{4}$$

With the help of q^* , the gray-level histogram of the image is re-normalized to deviate from equal probabilities as much as possible. This can result in a clearer representation of different clusters within the image, aiding in improving the quality of the image segmentation.

2.2. Multi-Level Thresholding Using Tsallis Entropy

Assuming that the gray-level histogram of an image is divided into $m+1$ parts by a set of thresholds $\vec{t} = (t_1, t_2, ..., t_m)$, denoted as $\vec{C} = (C_0, C_1, ..., C_m)$, after normalization, the probability distribution of each class is defined as:

$$\begin{gathered} C_0 : \frac{p_0}{P_0}, \frac{p_1}{P_0}, ..., \frac{p_{t_1}}{P_0} \\ \vdots \\ C_j : \frac{p_{t_j+1}}{P_j}, \frac{p_{t_j+2}}{P_j}, ..., \frac{p_{t_j}}{P_j}, \\ \vdots \\ C_m : \frac{p_{t_m+1}}{P_m}, \frac{p_{t_m+2}}{P_m}, ..., \frac{p_{L-1}}{P_m} \end{gathered} \tag{5}$$

where the cumulative probabilities of $m+1$ categories are defined as:

$$\begin{gathered} P_0 = \sum_{i=0}^{t_1} p_i \\ \vdots \\ P_j = \sum_{i=t_j+1}^{t_{j+1}} p_i, \\ \vdots \\ P_m = \sum_{i=t_m+1}^{L-1} p_i \end{gathered} \tag{6}$$

 doi:10.20944/preprints202408.0511.v1

Tsallis entropy of each region of $\vec{C} = (C_0, C_1, ..., C_m)$ is obtained by the following definition:

$$\begin{cases} S_q^0 = \left\{1 - \sum_{i=0}^{t_1} \left(\frac{p_i}{P_0}\right)^q\right\} \Big/ (q-1) \\ \vdots \\ S_q^j = \left\{1 - \sum_{i=t_j+1}^{t_{j+1}} \left(\frac{p_i}{P_j}\right)^q\right\} \Big/ (q-1). \\ \vdots \\ S_q^m = \left\{1 - \sum_{i=t_m+1}^{L-1} \left(\frac{p_i}{P_m}\right)^q\right\} \Big/ (q-1) \end{cases} \tag{7}$$

According to the pseudo-additivity property of Tsallis entropy, its multi-threshold objective function is defined as follows:

$$S_q(t_1, t_2, ..., t_m) = \sum_i S_q^i + (1-q) \sum_{j \neq k} S_q^j S_q^k + (1-q)^2 \sum_{u \neq v \neq w} S_q^u S_q^v S_q^w + ... + (1-q)^m \prod_{r=0}^{m} S_q^r. \tag{8}$$

Maximizing the objective function $S_q(t_1, t_2, ..., t_m)$ yields an optimal set of thresholds as follows:

$$\left(\vec{t}\right)^* = \arg\max\left\{S_q(t_1, t_2, ..., t_m)\right\}, \tag{9}$$

this algorithm is highly favored for its simplicity, intuitiveness, versatility, and excellent performance in image segmentation[33–35].

3. Image Test Sets and Quality Evaluation Parameters

There are lots of evidences showing that parameter q has deep relevance with the long-range interaction in bi-level image segmentation[24,30,31,36]. However, extending bi-level thresholding to multi-level thresholding and drawing the conclusions seems not so straight. In fact, it is found that if the backgrounds of the images are of random natural scenes, the above algorithm does not exhibit significant advantages in comparison with traditional Shannon algorithm and original Tsallis algorithm[12]. In order to further show the relevance between pixels' long-range correlations and nonextensivity during the imaging process, several different types of images are employed for comparison.

BSDS0500 is an image dataset consisting of randomly natural scenes. This dataset contains 500 images taken from real-world natural scenes, covering a variety of views and objects, including but not limited to modern urban landscapes, natural landscapes, animals and plants, human activities, and so on. These images provide diverse scenes and various visual information. Here are a few examples from this dataset.

Figure 1. Example images from the BSDS0500 image dataset

 doi:10.20944/preprints202408.0511.v1

INFRAIMGS1, INFRAIMGS2, INFRAIMGS3, and INFRAIMGS4 are series of image datasets containing lots of infrared images captured by fixed infrared cameras at different moments. These datasets record specific activities and movements of objects in different scenes.

- INFRAIMGS1: These images capture activities of pedestrians and vehicles on two fixed outdoor road scenes. The dataset consists of 464 images extracted from frames, with a resolution of 550×365 .
- INFRAIMGS2: This dataset depicts student activities at a fixed intersection near a teaching building. It comprises 264 images extracted from frames, with a resolution of 320×240 .
- INFRAIMGS3: Presenting scenes fixed inside a cabin, focusing on the movement of individuals in the area. This dataset contains 253 images extracted from frames, capturing scenes of interaction and movement between individuals, with a resolution of 320×240 .
- INFRAIMGS4: Showcasing scenes fixed in squares or similar open spaces, capturing pedestrians engaged in activities such as running, walking, or other leisure activities. The dataset comprises 118 images extracted from frames, with a resolution of 360×240.

CTIMGS is a collection of medical chest CT images covering scans of chests from different patients. These images have a fixed black background, and the dataset comprises a total of 600 images, with a resolution of 224×224 . Below are examples of images from these datasets.

In the same dataset of Figure 2, those images are taken from the same background and generated by the same imaging principle, i.e., infrared imaging for INFRAIMGS1-4 and X-ray imaging for CTIMGS. These specified types of images can help us to further understand the pixels' long-range correlations in imaging stage.

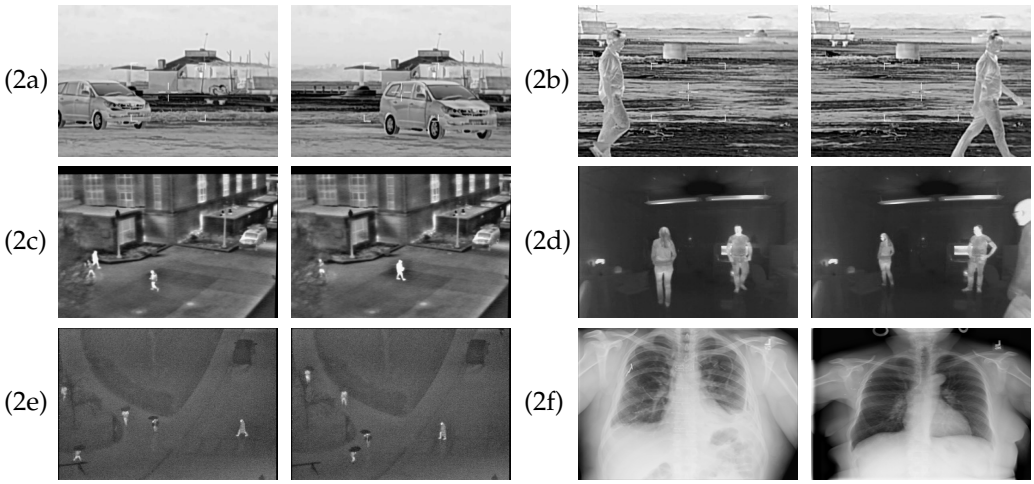

Figure 2. (**2a**) and (**2b**) are images in the image set INFRAIMGS1. (**2c**) are images in the image set INFRAIMGS2. (**2d**) are images in the image set INFRAIMGS3. (**2e**) are images in the image set INFRAIMGS4. (**2f**) are images in the image set CTIMGS.

In order to evaluate the effectiveness of this self-adaptive multi-level segmentation algorithm, PSNR (Peak Signal-to-Noise Ratio) and SSIM (Structural Similarity Index) are adopted as quality indices. PSNR[37] represents the ratio of the peak signal to the noise. In image multiple-thresholding, due to the gray-level compression, the output image is generally different from the original one. PSNR can precisely measure this difference and it is defined as:

$$PSNR = 10\log_{10}\left(\frac{255^2}{MSE}\right), \tag{10}$$

 doi:10.20944/preprints202408.0511.v1

MSE in Eq.(10) is the mean squared error between the output image and the input image, and 255 is the maximum gray-level value in the image in general. MSE can be written as:

$$MSE = \frac{1}{M \times N} \sum_{i=1}^{M} \sum_{j=1}^{N} [I(i,j) - K(i,j)]^2, \tag{11}$$

where $I(i,j)$ and $K(i,j)$ represent the original image and the image after segmentation, respectively.

The typical PSNR values in image segmentation range from 10 dB to 50 dB[38]. A higher PSNR value indicates a smaller distortion in the output image and higher quality of segmentation. PSNR closing to 50 dB indicates that the segmented image has very minor errors. If PSNR is greater than 30 dB, it is difficult for the human eyes to perceive differences between the segmented image and the original one. For PSNR ranging from 20 dB to 30 dB, the differences become noticeable to the human eyes. In the range of 10 dB to 20 dB, the differences become larger. Nevertheless, the human eyes can still recognize the main structures in the output image. If PSNR is below 10 dB, it becomes challenging for humans to determine if there are any correlations between the input and output images. PSNR is currently the most frequently used objective measure for evaluating image quality. However, many experimental results have shown that PSNR scores may not fully coincide with the visual quality perceived by the human eyes. It's possible for images with higher PSNR to appear worse visual quality than those with lower PSNR scores, since the human visual system's sensitivity to errors is affected by a lot of factors that more complicated than Eq.(10).

SSIM[39] is another quality metric that measuring the similarity between two digital images. The recognition criteria of human visual system, such as luminance, contrast, and structural information, are taken into account[40,41] to yield the expression of SSIM as:

$$SSIM(x,y) = \frac{(2\mu_x\mu_y + C_1)(2\sigma_{xy} + C_2)}{\left(\mu_x^2 + \mu_y^2 + C_1\right)\left(\sigma_x^2 + \sigma_y^2 + C_2\right)}, \tag{12}$$

where x and y represent the images before and after segmentation, μ_x and μ_y denote the mean intensity of the corresponding images, σ_x^2 and σ_y^2 represent the standard deviations respectively, σ_{xy} denotes the covariance of the images before and after segmentation, C_1 and C_2 are two constants to avoid zeros appearing in denominator. Eq.(12) shows that SSIM is a dimensionless value between 0 and 1, where smaller differences between the original and segmented images yield closer value to 1. Due to its simplicity and effectiveness, SSIM has been widely used in various applications related to image and video processing in recent years, such as image compression[42], image watermarking[43], wireless video streaming[44], and magnetic resonance imaging[45].

In practice, PSNR is more sensitive to additive Gaussian noise, while it exhibits lower sensitivity to JPEG compression. Conversely, SSIM is more sensitive to JPEG compression but relatively less responsive to additive Gaussian noise[46]. Therefore, we employ both PSNR and SSIM to assess the quality of the self-adaptive multi-level segmentation.

4. Experimental Results and Discussion

In order to show the detailed relevance between pixels' long-range correlations and non-extensive entropy index q within multi-level segmentation case, Shannon entropy and traditional Tsallis entropy are adopted as benchmarks to show the performance of the proposed self-adaptive algorithm. As mentioned above, Shannon entropy neglects the long-range correlations among image pixels and showing the extensive property. Tsallis entropy generalized the application scope of Shannon entropy by linking the strength of long-range correlations to non-extensive index q.

Images from the 6 datasets mentioned in section 3 are processed by using three different multi-level segmentation algorithms, i.e., Shannon, Tsallis (q=0.8), and proposed, to yield the optimal results respectively.

 doi:10.20944/preprints202408.0511.v1

Figure 3 shows the 4-level segmentation results of sample images from 6 datasets. For image from BSDS0500, the result of Shannon algorithm looks closest to the original image, which indicates that the long-range correlations among image pixels can be neglected. Since the images in BSDS0500 are generated from random scenes, it is inadequate to say that the pixels of different images should always exhibit the long-range correlation. However, for images from other 5 datasets, the segmentation results of proposed algorithm consistently show the superiority to the other two algorithms. Images in INFRAIMGS1-4 are generated by infrared cameras so that the infrared radiation plays important role during the imaging process. It is well known that infrared radiation depends closely on the temperature of the objects. Therefore, the patterns of pixels' long-range correlations actually reflect the temperature distributions of different objects in infrared images. And this kind of long-range correlation can be successfully captured by the self-adaptive multi-level segmentation algorithm, which is more flexible than the traditional Tsallis entropy with fixed q index. The evidence can also be found from the dataset of medical CT images, in which the pixels' gray-level directly depend on the absorption of X-ray by different organs inside human body. Therefore, the gray-level values of pixels belong to the same organ should have strong correlations and it is suitable to describe this kind of correlation by adaptive q index rather than fixed q.

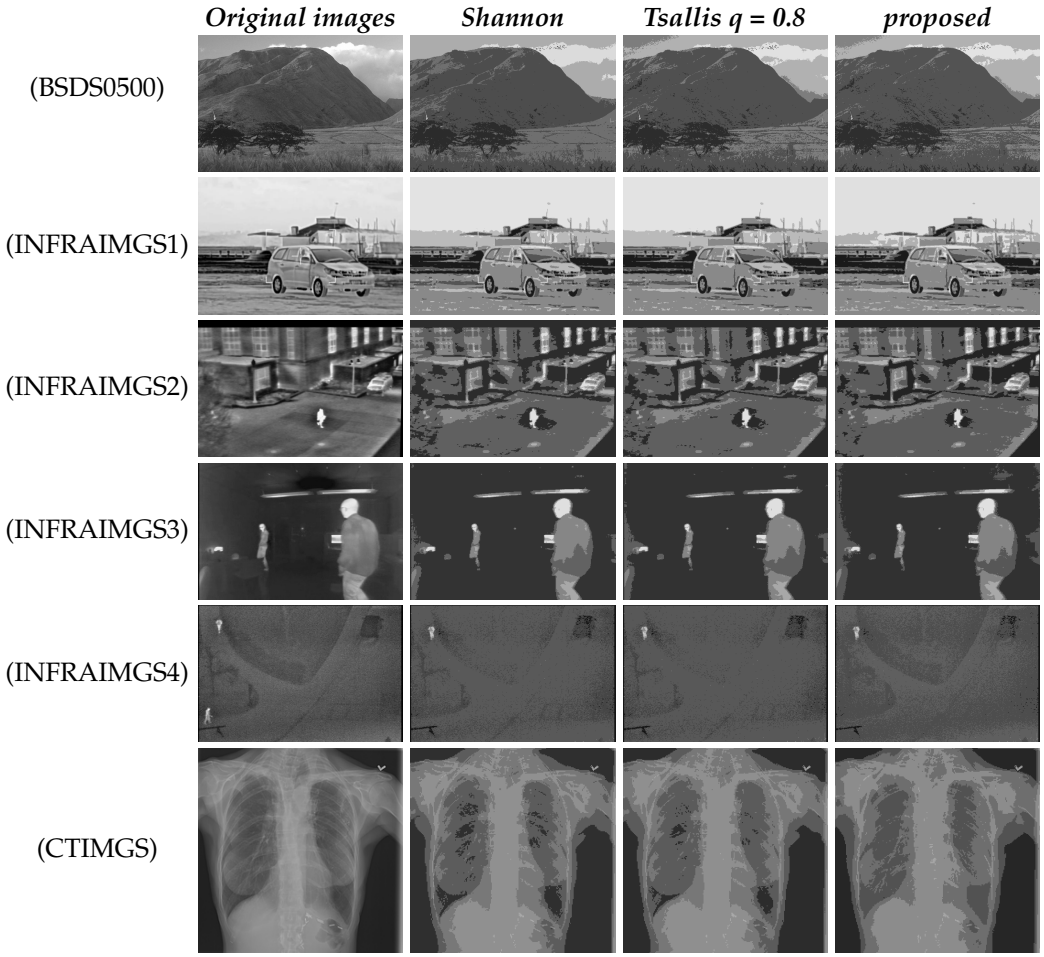

Figure 3. The 4-level segmentation results of the typical images from 6 datasets by using three different algorithms.

In order to show the segmentation results quantitatively, the output images of three algorithms are compared with the corresponding original images in terms of PSNR and SSIM. Table 1 shows part of the PSNR results of BSDS0500 images by using Shannon, Tsallis (q=0.8), and proposed muti-level thresholding algorithms, in which the number of thresholds is 4. In each line of Table 1, the maximum

 doi:10.20944/preprints202408.0511.v1

PSNR value (with bold font) indicates that the corresponding algorithm is the most suitable one for the image named at the beginning of the line.

Table 1. Part of PSNR results for images in BSDS0500 with different 4-level thresholding algorithms.

	Shannon	*Tsallis q=0.8*	*proposed*
BSDS00065	27.7979	27.8888	**28.0085**
BSDS00109	**28.0865**	**28.0865**	27.4921
BSDS00116	26.9156	**26.9787**	26.9286
BSDS00203	**29.1844**	29.0696	29.1492
BSDS00474	**29.5335**	29.3923	23.0752

Therefore, for all 500 images of BSDS0500 one can statistically obtain the most suitable rates of three algorithms. They are 32% for Shannon algorithm, 24.6% for Tsallis algorithm with q=0.8, and 55% for proposed self-adaptive algorithm. It is worth to mention that the sum of above three most suitable rates slightly exceeds 100%, because there are a few images, such as BSDS00109 in Table 1, happen to obtain the same best result by using different algorithms. Nevertheless, the probability of such case is small so that the images in other 5 datasets can be processed by the same way. And the statistical results are shown in Table 2.

Table 2. The most suitable rates of three algorithms suggested by PSNR for 6 datasets when the number of thresholds is 4.

	Shannon	*Tsallis q=0.8*	*proposed*
BSDS0500	32%	24.6%	55%
INFRAIMGS1	7.9%	13.1%	**84.3%**
INFRAIMGS2	0%	0%	**100%**
INFRAIMGS3	7.9%	13.8%	**87.3%**
INFRAIMGS4	14.1%	16.3%	**73.7%**
CTIMGS	14.1%	15.6%	**75.8%**

Interestingly, unlike the distribution of the most suitable rates in BSDS0500, all the other 5 datasets show a notable tendency (the corresponding rates are far larger than 65%) to the proposed algorithm. Especially for INFRAIMGS2, all of the 264 images in it recognize the self-adaptive q as the most suitable values to present the pixels' long-range correlations. The experimental results also show that the distribution of 264 q values ranges from 0.490 to 0.513, a very small interval. In fact, all images in INFRAIMGS2 have the same background and the ratios of foreground (moving objects) to the full image size are small. It is reasonable to say that the strength of long-range correlations in each image of this dataset should be quite similar, but cannot be empirically determined by a fixed value. Other datasets that have the same characteristics with INFRAIMGS2, all exhibit the consistency in the range of q. Such as $0.512 \leq q \leq 0.602$ for INFRAIMGS1, $0.509 \leq q \leq 0.580$ for INFRAIMGS3, $0.381 \leq q \leq 0.512$ for INFRAIMGS4. These behaviors coincide with the imaging principles mentioned above.

The validity of self-adaptive q can be further confirmed by SSIM. Table 3 shows part of the SSIM results for the same images adopted in Table 1 by using three different multi-level thresholding algorithms, in which the number of thresholds is still 4. Since the definition of SSIM is totally different from that of PSNR, their responses to the same output image may not always consistent with each other. Such as BSDS00116, according to the results of PSNR, Tsallis algorithm with q=0.8 is suggested as the most suitable one, while Shannon algorithm yields the highest SSIM score. Nevertheless, the statistical results of the most suitable rates suggested by SSIM can also be obtained in the same way as Table 2, and it is shown in Table 4.

 doi:10.20944/preprints202408.0511.v1

Table 3. Part of SSIM results for images in BSDS0500 with different 4-level thresholding algorithms.

	Shannon	*Tsallis q=0.8*	*proposed*
BSDS00065	**0.7484**	0.7466	0.7374
BSDS00109	**0.6423**	**0.6423**	0.6383
BSDS00116	**0.7257**	0.7237	0.7181
BSDS00203	0.7199	0.7185	**0.7205**
BSDS00474	**0.8066**	0.8063	0.7166

Table 4. The most suitable rates of three algorithms suggested by SSIM for 6 datasets when the number of thresholds is 4.

	Shannon	*Tsallis q=0.8*	*proposed*
BSDS0500	36.8%	23.2%	52.6%
INFRAIMGS1	12.7%	19.8%	**77.6%**
INFRAIMGS2	0%	0%	**100%**
INFRAIMGS3	10.6%	19.3%	**78.6%**
INFRAIMGS4	6.7%	16.9%	**89.8%**
CTIMGS	29.5%	25.8%	53.5%

The sum of the most suitable rate for each dataset also slightly exceeds 100%, and the reason is similar with that in Table 2. It is found that all of the infra image datasets show their preferences to the adaptive q as a measure of the strength of pixels' long-range correlations under the criterion of SSIM. The statistical result of INFRAIMGS2 is the most notable one. All of the images in it adopt the proposed algorithm to achieve the highest scores defined by not only PSNR but also SSIM. Besides Table 2 and Table 4, the results of the most suitable rates over 6 datasets can be extended to the cases of larger number of thresholds, as shown in Tables 5–8.

Table 5. The most suitable rates of three algorithms suggested by PSNR for 6 datasets when the number of thresholds is 5.

	Shannon	*Tsallis q=0.8*	*proposed*
BSDS0500	32.6%	28.2%	39.2%
INFRAIMGS1	21.3%	38.8%	**66.2%**
INFRAIMGS2	0%	0%	**100%**
INFRAIMGS3	19.3%	32.8%	53.4%
INFRAIMGS4	6.7%	16.9%	**89.8%**
CTIMGS	14.7%	15.7%	**75%**

Table 6. The most suitable rates of three algorithms suggested by SSIM for 6 datasets when the number of thresholds is 5.

	Shannon	*Tsallis q=0.8*	*proposed*
BSDS0500	34.6%	27.6%	50%
INFRAIMGS1	11.9%	22.2%	**87.1%**
INFRAIMGS2	0%	0%	**100%**
INFRAIMGS3	2.3%	8.6%	**93.3%**
INFRAIMGS4	2.5%	8.4%	**94.9%**
CTIMGS	30%	28.2%	50.3%

 doi:10.20944/preprints202408.0511.v1

Table 7. The most suitable rates of three algorithms suggested by PSNR for 6 datasets when the number of thresholds is 6.

	Shannon	*Tsallis q=0.8*	*proposed*
BSDS500	32%	30.2%	52.2%
INFRAIMGS1	20.9%	37.7%	**66.8%**
INFRAIMGS2	0%	0%	**100%**
INFRAIMGS3	40.7%	25.2%	40%
INFRAIMGS4	5.9%	11%	**89.8%**
CTIMGS	13.3%	18.6%	**74.5%**

Table 8. The most suitable rates of three algorithms suggested by SSIM for 6 datasets when the number of thresholds is 6.

	Shannon	*Tsallis q=0.8*	*proposed*
BSDS0500	38.4%	27.6%	48.8%
INFRAIMGS1	11.8%	21.7%	**87.1%**
INFRAIMGS2	0%	1.9%	**98.1%**
INFRAIMGS3	18.9%	32.4%	56.6%
INFRAIMGS4	5%	10.1%	**91.5%**
CTIMGS	27.5%	24%	56.2%

Tables 5 and 6 list the most suitable rates for 5-level segmentations to different datasets, where PSNR and SSIM are adopted as the criterions, respectively. And increasing the number of thresholds from 5 to 6, the results are listed in Tables 7 and 8. Impressively, images of INFRAIMGS2 show their robust preferences to the proposed algorithm in spite of the increasing number of thresholds. This kind of robustness can be also found in other datasets, such as INFRAIMGS1, INFRAIMGS4, CTIMGS. Therefore, it is suitable to adopt the self-adaptive q value to measure the strength of long-range correlations within images generated by known physical principles. In other words, the physical properties of objects shown in the images can be connected to the non-extensive parameter q by maximizing the redundancy of the histogram distribution. It is worth to mention that for INFRAIMGS3, the most suitable rate of proposed algorithm yields by PSNR keep decreasing when the number of thresholds grows. Since the gray-level gradations of images in INFRAIMGS3 are not plentiful, the increasing number of thresholds may lead to over segmentation and the results evaluated by PSNR and SSIM become unstable. Nevertheless, in most cases the proposed algorithm shows the effectiveness (with the most suitable rate higher than 65%) and robustness (keep fixed when the number of thresholds increases) in automatically detecting the long-range correlations among pixels of infrared images and medical images.

5. Conclusions

In image segmentation, determining the non-extensive parameter q of Tsallis entropy is an intriguing task. Since the value of q represents the strength of long-range interactions among pixels of the images that generated by some known physical principles, it cannot be determined empirically. At present paper, with the help of maximizing q-redundancy, we further study the connections between physical properties of objects shown in the images and the self-adaptive value of q in multi-threshold image segmentation. In comparison with Shannon entropy algorithm and traditional Tsallis entropy algorithm with q=0.8, it is found that the self-adaptive algorithm shows highly effectiveness and robustness to infrared images and medical CT images. The superiority and consistency of present algorithm are qualitatively illustrated by means of PSNR and SSIM when the number of thresholds is set as 4, 5, and 6, respectively. In addition, for a series of images that generated by the same process and sharing the same background, the long-range correlations pattern among pixels should be quite similar. And the self-adaptive q values of those images are also quite similar, as expected. All of

 doi:10.20944/preprints202408.0511.v1

these advantages will be helpful for the further applications of Tsallis entropy in multi-level image segmentation.

Author Contributions: Conceptualization, C.O. and K.Z.; methodology, C.O.; software, K.Z.; validation, K.Z. and M.H.; formal analysis, C.O. and K.Z.; investigation, K.Z. and L.D.; resources, L.D.; data curation, K.Z.; writting—original draft preparation, K.Z.; writing—review and editing, C.O.; visualization, K.Z.; supervision, C.O.. All authors have read and agreed to the published version of the manuscript.

Funding: The authors would like to thank the support by the National Natural Science Foundation of China (No. 11775084), the Program for prominent Talents in Fujian Province, and Scientific Research Foundation for the Returned Overseas Chinese Scholars.

Data Availability Statement: The original contributions presented in the study are included in the article, further inquiries can be directed to the corresponding author.

Acknowledgments: The authors would like to thank https://www2.eecs.berkeley.edu, http://vcipl-okstate.org/pbvs/bench/ and https://wiki.cancerimagingarchive.net/display/Public/CT+Images+in+COVID-19 for providing source images.

Conflicts of Interest: The authors declare no conflict of interest.

References

1. Hosny, K.M.; Khalid, A.M.; Hamza, H.M.; Mirjalili, S. Multilevel thresholding satellite image segmentation using chaotic coronavirus optimization algorithm with hybrid fitness function. *Neural Computing and Applications* **2023**, *35*, 855–886, https://doi.org/10.1007/s00521-022-07718-z.
2. Abualigah, L.; Habash, M.; Hanandeh, E.S.; Hussein, A.M.; Shinwan, M.A.; Zitar, R.A.; Jia, H. Improved reptile search algorithm by salp swarm algorithm for medical image segmentation. *Journal of Bionic Engineering* **2023**, *20*, 1766–1790, https://doi.org/10.1007/s42235-023-00332-2.
3. Xing, Z.; He, Y. Many-objective multilevel thresholding image segmentation for infrared images of power equipment with boost marine predators algorithm. *Applied Soft Computing* **2021**, *113*, 107905, https://doi.org/10.1016/j.asoc.2021.107905.
4. Khudov, H.; Makoveichuk, O.; Butko, I.; Gyrenko, I.; Stryhun, V.; Bilous, O.; Shamrai, N.; Kovalenko, A.; Khizhnyak, I.; Khudov, R. Devising a method for segmenting camouflaged military equipment on images from space surveillance systems using a genetic algorithm. *Eastern-European Journal of Enterprise Technologies* **2022**, *117*, 9, https://doi.org/10.15587/1729-4061.2022.259759.
5. Iannizzotto, G.; Vita, L. Fast and accurate edge-based segmentation with no contour smoothing in 2-D real images. *IEEE Transactions on Image Processing* **2000**, *9*, 1232–1237, https://doi.org/10.1109/83.847835.
6. Wang, L.; Yu, B.; Chen, F.; Li, C.; Li, B.; Wang, N. A cluster-based partition method of remote sensing data for efficient distributed image processing. *Remote Sensing* **2022**, *14*, 4964, https://doi.org/10.3390/rs14194964.
7. Tang, J. A color image segmentation algorithm based on region growing. In *Proceedings of the 2010 2nd International Conference on Computer Engineering and Technology*; IEEE: 2010; Volume 6, pp. V6–634, https://doi.org/10.1109/ICCET.2010.5486012.
8. Pun, T. A new method for grey-level picture thresholding using the entropy of the histogram. *Signal Processing* **1980**, *2*, 223–237, https://doi.org/10.1016/0165-1684(80)90020-1.
9. Kapur, J. N.; Sahoo, P. K.; Wong, A. K. C. A new method for gray-level picture thresholding using the entropy of the histogram. *Computer Vision, Graphics, and Image Processing* **1985**, *29*, 273–285, https://doi.org/10.1016/0734-189X(85)90125-2.
10. Agrawal, S.; Panda, R.; Bhuyan, S.; Panigrahi, B. K. Tsallis entropy based optimal multilevel thresholding using cuckoo search algorithm. *Swarm and Evolutionary Computation* **2013**, *11*, 16–30, https://doi.org/10.1016/j.swevo.2013.02.001.
11. Bhandari, A. K.; Kumar, A.; Singh, G. K. Tsallis entropy based multilevel thresholding for colored satellite image segmentation using evolutionary algorithms. *Expert Systems with Applications* **2015**, *42*, 8707–8730, https://doi.org/10.1016/j.eswa.2015.07.025.
12. Sharma, A.; Chaturvedi, R.; Kumar, S.; Dwivedi, U. K. Multi-level image thresholding based on Kapur and Tsallis entropy using firefly algorithm. *Journal of Interdisciplinary Mathematics* **2020**, *23*, 563–571, https://doi.org/10.1080/09720502.2020.1731976.

 doi:10.20944/preprints202408.0511.v1

13. Zhao, D.; Liu, L.; Yu, F.; Heidari, A. A.; Wang, M.; Oliva, D.; Muhammad, K.; Chen, H. Ant colony optimization with horizontal and vertical crossover search: Fundamental visions for multi-threshold image segmentation. *Expert Systems with Applications* **2021**, *167*, 114122, https://doi.org/10.1016/j.eswa.2020.114122.
14. Abdel-Basset, M.; Mohamed, R.; AbdelAziz, N. M.; Abouhawwash, M. HWOA: A hybrid whale optimization algorithm with a novel local minima avoidance method for multi-level thresholding color image segmentation. *Expert Systems with Applications* **2022**, *190*, 116145, https://doi.org/10.1016/j.eswa.2021.116145.
15. Wang, S.; Fan, J. Simplified expression and recursive algorithm of multi-threshold Tsallis entropy. *Expert Systems with Applications* **2024**, *237*, 121690, https://doi.org/10.1016/j.eswa.2023.121690.
16. Pathria, R. K. *Statistical Mechanics*, 2nd, ed.; Elsevier (Singapore) Pte Ltd: China, 2001; pp. 9–28, ISBN 981-4095-20-6.
17. Shannon, C. E. A mathematical theory of communication. *The Bell System Technical Journal* **1948**, *27*, 379–423, https://doi.org/10.1002/j.1538-7305.1948.tb01338.x.
18. Tsallis, C. Possible generalization of Boltzmann-Gibbs statistics. *Journal of Statistical Physics* **1988**, *52*, 479–487, https://doi.org/10.1007/BF01016429.
19. Tsallis, C. I. Nonextensive statistical mechanics and thermodynamics: Historical background and present status. In *Nonextensive Statistical Mechanics and Its Applications*; Springer: 2001; pp. 3–98, https://doi.org/10.1007/3-540-40919-X_1.
20. Tsallis, C. Inter-occurrence times and universal laws in finance, earthquakes and genomes. *Chaos, Solitons & Fractals* **2016**, *88*, 254–266, https://doi.org/10.1016/j.chaos.2015.12.025.
21. Sigalotti, L. D. G.; Ramírez-Rojas, A.; Vargas, C. A. Tsallis q-Statistics in Seismology. *Entropy* **2023**, *25*, 408, https://doi.org/10.3390/e25030408.
22. Pavlos, G. P.; Karakatsanis, L. P.; Iliopoulos, A. C.; Pavlos, E. G.; Xenakis, M. N.; Clark, P.; Duke, J.; Monos, D. S. Measuring complexity, nonextensivity and chaos in the DNA sequence of the Major Histocompatibility Complex. *Physica A: Statistical Mechanics and its Applications* **2015**, *438*, 188–209, https://doi.org/10.1016/j.physa.2015.06.044.
23. Zhang, Q.; Luo, C.; Li, M.; Deng, Y.; Mahadevan, S. Tsallis information dimension of complex networks. *Physica A: Statistical Mechanics and its Applications* **2015**, *419*, 707–717, https://doi.org/10.1016/j.physa.2014.10.071.
24. De Albuquerque, M. P.; Esquef, I. A.; Mello, A. R. G. Image thresholding using Tsallis entropy. *Pattern Recognition Letters* **2004**, *25*, 1059–1065, https://doi.org/10.1016/j.patrec.2004.03.003.
25. Bhandari, A. K.; Kumar, A.; Singh, G. K. Tsallis entropy based multilevel thresholding for colored satellite image segmentation using evolutionary algorithms. *Expert Systems with Applications* **2015**, *42*, 8707–8730, https://doi.org/10.1016/j.eswa.2015.07.025.
26. Raja, N. S. M.; Fernandes, S. L.; Dey, N.; Satapathy, S. C.; Rajinikanth, V. Contrast enhanced medical MRI evaluation using Tsallis entropy and region growing segmentation. *Journal of Ambient Intelligence and Humanized Computing* **2024**, pp. 1–12, https://doi.org/10.1007/s12652-018-0854-8.
27. Tsallis, C. Nonextensive Statistical Mechanics: Construction and Physical Interpretation. In *TNonextensive Entropy: Interdisciplinary Applications*; Gell-Mann, M.; Tsallis, C., Eds.; Oxford University Press:, 198 Madison Avenue, New York, New York 10016, 2004; pp. 2–55, ISBN 0-19-515976-4.
28. Tsallis, C. Nonadditive entropy and nonextensive statistical mechanics—an overview after 20 years. *Brazilian Journal of Physics* **2009**, *39*, 337–356, https://doi.org/10.1590/S0103-97332009000400002.
29. Rodrigues, P. S.; Giraldi, G. A. Computing the q-index for Tsallis nonextensive image segmentation. In *2009 XXII Brazilian Symposium on Computer Graphics and Image Processing*; IEEE: 2009; pp. 232–237, https://doi.org/10.1109/SIBGRAPI.2009.23.
30. Ramírez-Reyes, A.; Hernández-Montoya, A. R.; Herrera-Corral, G.; Domínguez-Jiménez, I. Determining the entropic index q of Tsallis entropy in images through redundancy. *Entropy* **2016**, *18*, 299, https://doi.org/10.3390/e18080299.
31. Deng, Q.; Shi, Z.; Ou, C. Self-adaptive image thresholding within nonextensive entropy and the variance of the gray-level distribution. *Entropy* **2022**, *24*, 319, https://doi.org/10.3390/e24030319.
32. dos Santos, R. J. V. Generalization of Shannon's theorem for Tsallis entropy. *Journal of Mathematical Physics* **1997**, *38*, 4104–4107, https://doi.org/10.1063/1.532107.

33. Naidu, M.S.R.; Kumar, P.R.; Chiranjeevi, K. Shannon and fuzzy entropy based evolutionary image thresholding for image segmentation. *Alexandria Engineering Journal* **2018**, *57*, 1643–1655, https://doi.org/10.1016/j.aej.2017.05.024.
34. Zou, Y.; Zhang, J.; Upadhyay, M.; Sun, S.; Jiang, T. Automatic image thresholding based on Shannon entropy difference and dynamic synergic entropy. *IEEE Access* **2020**, *8*, 171218–171239, https://doi.org/10.1109/ACCESS.2020.3024718.
35. Ifan Roy Thanaraj, R.; Anand, B.; Allen Rahul, J.; Rajinikanth, V. Appraisal of breast ultrasound image using Shannon's thresholding and level-set segmentation. In Proceedings of ICCAN 2019; Progress in Computing, Analytics and Networking; Springer, 2020; pp. 621–630, https://doi.org/10.1007/978-981-15-2414-1_62.
36. Lin, Q.; Ou, C. Tsallis entropy and the long-range correlation in image thresholding. *Signal Processing* **2012**, *92*, 2931–2939, https://doi.org/10.1016/j.sigpro.2012.05.025.
37. Hore, A.; Ziou, D. Image quality metrics: PSNR vs. SSIM. In *2010 20th International Conference on Pattern Recognition*; IEEE: 2010; pp. 2366–2369, https://doi.org/10.1109/ICPR.2010.579.
38. Sheikh, H. R.; Bovik, A. C. Image information and visual quality. *IEEE Transactions on Image Processing* **2006**, *15*, 430–444, https://doi.org/10.1109/TIP.2005.859378.
39. Wang, Z.; Bovik, A. C.; Sheikh, H. R.; Simoncelli, E. P. Image quality assessment: From error visibility to structural similarity. *IEEE Transactions on Image Processing* **2004**, *13*, 600–612, https://doi.org/10.1109/TIP.2003.819861.
40. Wang, Z.; Bovik, A. C. Mean squared error: Love it or leave it? A new look at signal fidelity measures. *IEEE Signal Processing Magazine* **2009**, *26*, 98–117, https://doi.org/10.1109/MSP.2008.930649.
41. Sheikh, H. R.; Sabir, M. F.; Bovik, A. C. A statistical evaluation of recent full reference image quality assessment algorithms. *IEEE Transactions on Image Processing* **2006**, *15*, 3440–3451, https://doi.org/10.1109/TIP.2006.881959.
42. Richter, T.; Kim, K. J. A MS-SSIM optimal JPEG 2000 encoder. In *2009 Data Compression Conference*; IEEE: 2009; pp. 401–410, https://doi.org/10.1109/DCC.2009.15.
43. Alattar, A. M.; Lin, E. T.; Celik, M. U. Digital watermarking of low bit-rate advanced simple profile MPEG-4 compressed video. *IEEE Transactions on Circuits and Systems for Video Technology* **2003**, *13*, 787–800, https://doi.org/10.1109/TCSVT.2003.815958.
44. Vukadinovic, V.; Karlsson, G. Trade-offs in bit-rate allocation for wireless video streaming. *IEEE Transactions on Multimedia* **2009**, *11*, 1105–1113, https://doi.org/10.1109/TMM.2009.2026096.
45. Reinsberg, S. A.; Doran, S. J.; Charles-Edwards, E. M.; Leach, M. O. A complete distortion correction for MR images: II. Rectification of static-field inhomogeneities by similarity-based profile mapping. *Physics in Medicine & Biology* **2005**, *50*, 2651, https://doi.org/10.1088/0031-9155/50/11/014.
46. Hore, A.; Ziou, D. Image quality metrics: PSNR vs. SSIM. In *2010 20th International Conference on Pattern Recognition*; IEEE: 2010; pp. 2366–2369, https://doi.org/10.1109/ICPR.2010.579.